Title
Tests of diffusion-free scaling behaviors in numerical dynamo datasets

Authors
Cheng, JS
Aurnou, JM

Publication Date
2016-02-01

DOI
10.1016/j.epsl.2015.12.004

Peer reviewed

Earth and Planetary Science Letters 436 (2016) 121–129

Contents lists available at ScienceDirect

Earth and Planetary Science Letters

www.elsevier.com/locate/epsl

Tests of diffusion-free scaling behaviors in numerical dynamo datasets

J.S. Cheng *, J.M. Aurnou

Dept. of Earth, Planetary and Space Sciences, University of California – Los Angeles, CA, USA

ARTICLE INFO

Article history:
Received 22 July 2015
Received in revised form 22 November 2015
Accepted 14 December 2015
Available online 30 December 2015
Editor: B. Buffett

Keywords:
fluid dynamics
dynamo simulations
heat transfer
non-dimensional scalings
outer core
rotating convection

ABSTRACT

Many dynamo studies extrapolate numerical model results to planetary conditions by empirically constructing scaling laws. The seminal work of Christensen and Aubert (2006) proposed a set of scaling laws that have been used throughout the geoscience community. These scalings make use of specially-constructed parameters that are independent of fluid diffusivities, anticipating that large-scale turbulent processes will dominate the physics in planetary dynamo settings. With these 'diffusion-free' parameterizations, the results of current numerical dynamo models extrapolate directly to fully-turbulent planetary core systems; the effects of realistic fluid properties merit no further investigation. In this study, we test the validity of diffusion-free heat transfer scaling arguments and their applicability to planetary conditions. We do so by constructing synthetic heat transfer datasets and examining their scaling properties alongside those proposed by Christensen and Aubert (2006). We find that the diffusion-free parameters compress and stretch the heat transfer data, eliminating information and creating an artificial alignment of the data. Most significantly, diffusion-free heat transfer scalings are found to be unrelated to bulk turbulence and are instead controlled by the onset of non-magnetic rotating convection, itself determined by the viscous diffusivity of the working fluid. Ultimately, our results, in conjunction with those of Stelzer and Jackson (2013) and King and Buffett (2013), show that diffusion-free scalings are not validated by current-day numerical dynamo datasets and cannot yet be extrapolated to planetary conditions.

1. Introduction

The Earth's magnetic field is generated by dynamo action in the liquid metal outer core. Much of our understanding of the geodynamo comes from direct numerical simulations that solve the governing equations of magnetohydrodynamic flow in a rotating spherical shell of conducting fluid (e.g., Glatzmaier, 2013). Numerical models attempt to reproduce key features of the observed field, such as the dipolar morphology and polarity reversals, and link these features to flow behaviors (e.g., Glatzmaier and Coe, 2007; Aubert et al., 2008; Olson et al., 2011). However, limitations in computational power preclude these models from being run with parameter values similar to those that exist in the core. Applying the results of models to the core therefore requires massive extrapolation through parameter space. A prevalent method to achieve this extrapolation is to empirically determine power law scaling relations between the governing parameters. These scaling laws are constructed by conducting large surveys of dynamo models within achievable parameter ranges. These scalings are then extrapolated from presently-accessible parameter values to planetary-scale estimates.

In the fluid physics community, the so-called ultimate regime of convective turbulence has been theorized and searched for extensively (e.g., Kraichnan, 1962; Spiegel, 1971; Ahlers et al., 2009; Roche et al., 2010; Grossmann and Lohse, 2011; Julien et al., 2012b; He et al., 2014). In this ultimate regime, it is hypothesized that the fluid's molecular diffusivities do not contribute meaningfully to the physics, and instead only macro-scale turbulent phenomena dictate the flow behaviors. In order to extrapolate dynamo results to the core, Christensen and Aubert (2006) aimed to produce analogous asymptotic scalings for dynamo physics. These scaling laws have been widely used in the recent geoscience literature (e.g., Aubert et al., 2009, 2010; Tarduno et al., 2012; Driscoll and Bercovici, 2013), the planetary science literature (e.g., Christensen, 2002; Hauck et al., 2006; Olson and Christensen, 2006; Aurnou, 2007; Takahashi et al., 2008; Christensen et al., 2009, 2010; Schmitz and Tilgner, 2010; Weiss et al., 2010; Aurnou and Aubert, 2011; Christensen, 2011; Showman et al., 2011; Davidson, 2013; Yadav et al., 2013a, 2013b; Davidson, 2014; Dharmaraj et al., 2014; Garcia et al., 2014; Laneuville et al., 2014; Schrinner et al., 2014; Tilgner, 2014; Christensen, 2015), and the exoplanetary science literature (e.g., Gaidos et al., 2010;

* Corresponding author.
E-mail address: jscheng07@g.ucla.edu (J.S. Cheng).

http://dx.doi.org/10.1016/j.epsl.2015.12.004
0012-821X/

Driscoll and Olson, 2011; Summeren et al., 2013; Zuluaga et al., 2013).

However, in contrast to the extreme parameters which must be reached to observe the asymptotic behavior in other convection systems, dynamo models are presently restricted to rather moderate parameter ranges. It may be the case that the addition of rotational forces and magnetic fields allow asymptotic behaviors to be reached at less extreme parameters. However, these predictions must be verified before claims of achieving an ultimate dynamo physics regime can be made (e.g., Julien et al., 2012b; King and Buffett, 2013).

Stelzer and Jackson (2013) demonstrate that a statistically-significant improvement can be made to Christensen and Aubert (2006)'s scaling laws for flow velocity and magnetic field strength by reintroducing a dependence on viscous and magnetic diffusivities. Thus, they show that diffusion-free empirical fits do not optimally describe flow and magnetic field outputs from present-day dynamo models. Stelzer and Jackson show this via a leave-one-out cross-validation (LOOCV) method, applied to 116 dynamo cases from Christensen and Aubert (2006)'s and following papers. In the LOOCV method, a single case is isolated at a time and a scaling law is constructed from the remaining cases, assuming a power-law relationship between relevant governing parameters. The scaling law is evaluated for its ability to predict the isolated case, and the process is repeated for each case. Using this statistical method, Stelzer and Jackson (2013)'s results make clear that flow and magnetic fields in present-day dynamo models are not yet following a diffusion-free physics, as may be the case in extreme geophysical and astrophysical turbulent flows.

Unlike all other tested quantities, Stelzer and Jackson (2013) find that the heat transfer data are indeed best fit by a diffusion-free scaling relation. Since heat transfer is a globally integrated descriptor of the convection dynamics (e.g., Glazier, 1999), it can be argued that the heat transfer in dynamo models is the first quantity to develop a diffusion-free behavior. It could then be argued that since the heat transfer is following diffusion-free physics, the other quantities will eventually do so as well.

In this paper, however, we show that the goodness of fit of heat transfer data to the scaling proposed in Christensen and Aubert (2006) is determined *a priori* by the way the diffusion-free parameters are defined, rather than by the underlying dynamo physics. In particular, we show that the heat transfer scaling is determined by the onset of convection, which is, in turn, determined by the viscous diffusivity of the fluid. We therefore demonstrate that the scaling is not diffusion-free, contrary to the preconditions for diffusion-free parameters to be applicable.

In Section 2, we define the diffusive and diffusion-free non-dimensional parameters relevant to heat transfer. In Section 3, we introduce the concepts of flattening and shingling that cause the heat transfer data to conform to the onset scaling. We illustrate these concepts using synthetic heat transfer datasets that resemble real dynamo model data. In Section 4, we demonstrate that these concepts lead to a loss of scaling information when real dynamo model data are plotted in diffusion-free parameter space. Regardless of variations in the scaling data, the best-fit scaling that emerges in diffusion-free parameter space is the same. Our results show that data from present-day dynamo models do not provide support for asymptotically-accurate diffusion-free heat transfer physics. Instead, the best fit trend is controlled by the onset of convection in these experiments and has little to do with the bulk turbulent dynamics expected to underly diffusion-free systems (e.g., Julien et al., 2012a).

2. Heat transfer parametrization

2.1. Diffusive parameters

In core dynamics, flows are traditionally described by the magnetohydrodynamic equations that are non-dimensionalized by the relevant time-scales in the problem (e.g., the diffusion times, convection time scale, rotation time, and magnetic induction time scale). This operation generates a (non-unique) set of non-dimensional numbers that are ratios of these various characteristic time scales. Scaling laws associated with heat transfer depend on the Rayleigh number Ra, the Nusselt number Nu, the Prandtl and magnetic Prandtl numbers Pr and Pm, as well as the Ekman number E (e.g., Incropera and DeWitt, 1985; Gubbins and Roberts, 1987; Bergman et al., 2011).

The definitions of Ra, Pr, Pm and E depend on diffusive time scales. Viscous and thermal diffusion time scales are defined respectively as:

$$\tau_\nu = L^2/\nu\,, \quad \tau_\kappa = L^2/\kappa\,, \tag{1}$$

where L is a characteristic length, ν is the viscous diffusivity, and κ is the thermal diffusivity. The time scale for buoyancy forcing τ_{ff} is associated with the convective free-fall velocity of a fluid parcel U_{ff}. This is derived by balancing the inertial term with thermal buoyancy force:

$$\begin{aligned} \vec{u}\cdot\vec{\nabla}\vec{u} \sim \alpha_T \Delta T \vec{g} \quad &\rightarrow \quad U_{ff}(U_{ff}/L) \sim \alpha_T \Delta T g \\ &\rightarrow \quad U_{ff} = (\alpha_T g \Delta T L)^{1/2}\,. \end{aligned}$$

Thus,

$$\tau_{ff} = \frac{L}{U_{ff}} = \left(\frac{L}{\alpha_T g \Delta T}\right)^{1/2}, \tag{2}$$

where α_T is the thermal expansivity coefficient, g is gravitational acceleration and ΔT is the adverse temperature gradient in the fluid.

The Rayleigh number compares the time scales of viscous and thermal diffusivities to that of the free-fall buoyancy time scale:

$$Ra = \frac{\tau_\nu}{\tau_{ff}}\frac{\tau_\kappa}{\tau_{ff}} = \frac{\alpha_T g \Delta T L^3}{\nu\kappa}\,. \tag{3}$$

Rayleigh–Bénard convection (non-rotating, non-magnetic) onsets after a critical value of $Ra \sim 10^3$ (Chandrasekhar, 1961).

The Prandtl number is defined by the ratio between thermal diffusion and viscous diffusion time scales, and is given by:

$$Pr = \frac{\tau_\kappa}{\tau_\nu} = \frac{\nu}{\kappa}\,. \tag{4}$$

While core dynamo regions are estimated to have Pr values between 10^{-1} and 10^{-2} (Pozzo et al., 2012; Davies et al., 2015; Zhang et al., 2015), the majority of dynamo models are carried out at $Pr = 1$ due to computational constraints.

The magnetic Prandtl number is defined by the ratio between magnetic diffusion and viscous diffusion time scales, and is given by:

$$Pm = \frac{\tau_\eta}{\tau_\nu} = \frac{\nu}{\eta} = \mu_0 \nu \sigma\,, \tag{5}$$

where $\tau_\eta = L^2/\eta$; $\eta = (\mu_0\sigma)^{-1}$ is the magnetic diffusivity, σ is the fluid's electrical conductivity and μ_0 is the permeability of free space. Planetary dynamo generating regions are estimated to have Pm values of order 10^{-6} to 10^{-8} (Schubert and Soderlund, 2011). In contrast, for the fluid to be sufficiently inductive to produce dynamo action, the majority of present-day dynamo models must be carried out at $Pm \simeq 1$ (Aurnou et al., 2015).

The Nusselt number, Nu, represents the efficiency of heat transfer in a system. It is given by the ratio of the conductive heat transfer time scale and the total heat transfer time scale. The conductive heat transfer time scale is equivalent to thermal diffusion time scale, τ_κ, and is equivalent to the time it takes a given thermal energy anomaly to be diffusively transferred across a fluid layer of length L. The total heat transfer time scale is:

$$\tau_q = \rho C_p \Delta T \cdot \left(\frac{q}{L}\right)^{-1} = \frac{\rho C_p \Delta T L}{q}, \tag{6}$$

where q is the total (diffusive + advective) heat flux per unit area, ρ is the density and C_p is the heat capacity. This is the time it takes for a given thermal energy anomaly $\rho C_p \Delta T$ to be transferred across a system of length L by both advection and diffusion. The Nusselt number is then written as:

$$Nu = \frac{\tau_\kappa}{\tau_q} = \frac{qL}{\kappa \rho C_p \Delta T}. \tag{7}$$

The onset of convection is associated with a Nu value of 1, since, prior to onset, all of the heat is transported via conduction. In contrast, for most solar system planets with dynamos, the (superadiabatic) Nusselt number can be roughly estimated at $O(10^5)$ or greater (Cheng et al., 2015).

In rotating systems, the characteristic rotational time scale is $\tau_\Omega = 1/\Omega$, where Ω is the system angular rotation rate. The Ekman number is the ratio of the rotational and viscous time scales:

$$E = \frac{\tau_\Omega}{\tau_\nu} = \frac{\nu}{\Omega L^2}. \tag{8}$$

In planetary bodies, E is extremely small, around $O(10^{-15})$ (Table 2). For presently achievable parameters in dynamo modeling, the minimum E is approximately 10 orders of magnitude larger than estimates for planets.

Convection in rotating systems first onsets at a critical value of the Rayleigh number that varies as a function of both the rotation rate Ω of the system, and, importantly, the viscosity of the fluid. The critical Rayleigh number for the onset of steady rotating convection is given by:

$$Nu = 1, \quad Ra_{crit} = c_1 E^{-4/3} \tag{9}$$

where $c_1 = 8.7$ in a plane layer as $E \to 0$ (Chandrasekhar, 1961).

In dynamo models carried out at the same E value, convection first onsets at values close to Ra_{crit} as defined in (9) (e.g., King et al., 2010; Soderlund et al., 2012). As Ra/Ra_{crit} is increased while holding E constant, the Nu and Ra data are often found to follow an approximate power law scaling of the form:

$$Nu = \left(\frac{Ra}{Ra_{crit}}\right)^\alpha, \tag{10}$$

where the scaling exponent α is a non-negative constant (King et al., 2010; Julien et al., 2012a; Cheng et al., 2015). We refer to all data sharing the same Ekman number value as a single E-dataset.

The relations (9) and (10) are based on predictions for non-magnetic, plane-layer rotating convection. In current day dynamo models, the heat transfer behaviors are rather similar to non-magnetic rotating systems. Extending the best fit trends for each E-dataset to $Nu = 1$ in Christensen and Aubert (2006)'s data gives that the critical Rayleigh number values roughly follow a scaling of $Ra_{crit} = 6.5E^{-4/3}$, where we have not considered a small "tail" in the data near convective onset (e.g., see Yadav et al., 2015). This is consistent with the form given by (9). In our synthetic data, we use a prefactor of $c_1 = 8.7$ for simpler comparison with theory (e.g., Chandrasekhar, 1961).

Fig. 1a is a schematic showing the Nusselt and Rayleigh number ranges covered by synthetic hypothetical E-datasets. The synthetic data overlap with the parameter ranges achievable by present-day models, ranging from Ekman numbers of 3×10^{-4} to 3×10^{-6}. At each Ekman number, we plot an E-dataset containing ten data points, spaced evenly in log space, following a power law trend $\alpha = 3.5$ for approximately one decade in Nu. The lower bound of each E-dataset is set by the onset of convection, $Nu_{crit} = 1$, denoted by the solid horizontal line.

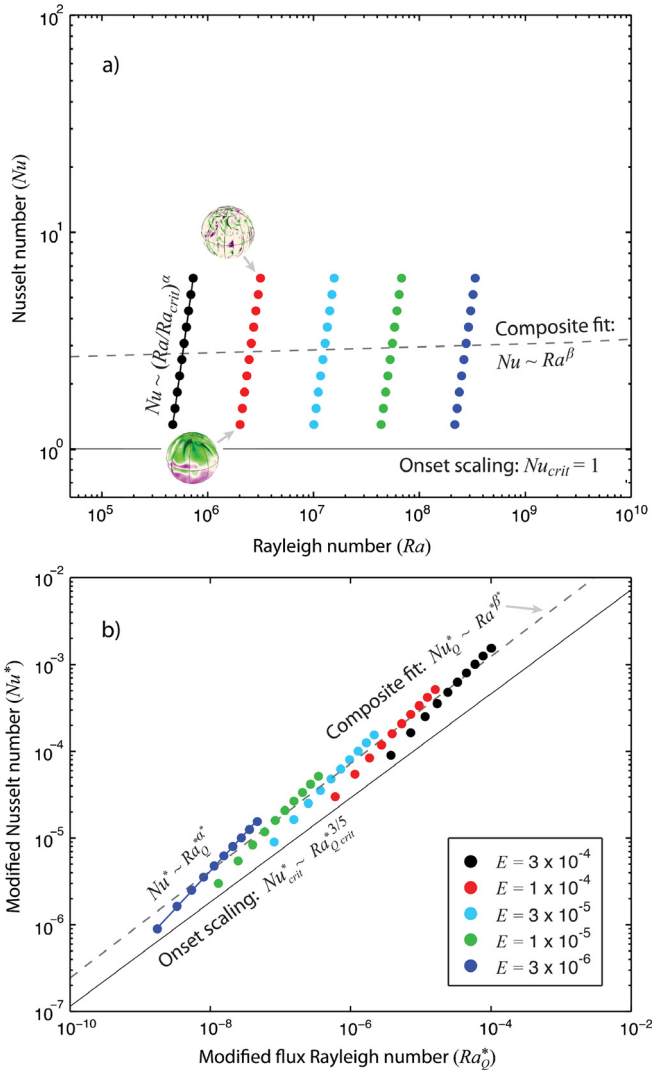

Fig. 1. a) Synthetic heat transfer (Nu) versus buoyancy forcing (Ra) datasets for rotating convection problems with non-dimensional rotation periods of $E = 3 \times 10^{-4}$ to $E = 10^{-6}$. Using (10), $\alpha = 3.5$ is given for the synthetic data. Convection onsets at critical Rayleigh number $Ra_{crit} \simeq 8.7E^{-4/3}$ and constant Nusselt number $Nu = 1$. The 'composite fit' is given by $\beta = 0.01$ (coefficient of determination $R^2 = 0.004$). b) Schematic showing the diffusion-free heat transfer (Nu^*) versus diffusion-free buoyancy forcing (Ra_Q^*) corresponding to the same data as in panel a. The diffusion-free analogue to α is given by α^*. Following (16), the convective onset slope is given by $Nu^* \sim Ra_Q^{*3/5}$. The diffusion-free 'composite fit' is given by $\beta^* = 0.63$ (coefficient of determination $R^2 = 0.98$). The color images in Fig. 1a show examples of outer boundary radial magnetic fields in dynamo models (e.g., Soderlund et al., 2012). (For interpretation of the references to color in this figure legend, the reader is referred to the web version of this article.)

The color images in Fig. 1a show characteristic magnetic field morphologies in $E = 10^{-4}$ dynamo cases from Soderlund et al. (2012). At low Ra/Ra_{crit}, current day dynamo models typically produce dipolar fields. At $Ra/Ra_{crit} \gtrsim 10$, buoyancy-driven inertial forces overcome Coriolis forces and the magnetic field signal becomes broadband, typically with multipolar field morphologies (Kutzner and Christensen, 2002; Sreenivasan and Jones, 2011; Soderlund et al., 2012; Dharmaraj et al., 2014). Furthermore, when

Table 1
Material and dynamical property estimates for solar system planets used in Section 2. The material property estimates are all given for the top of the dynamo generating region, denoted by R_D. Below, R_P is the planetary radius, L is the thickness of the dynamo generating region and q_{sa} is the superadiabatic heat flux estimated at $r = R_D$. Sources are: [1] Redmond and King (2007); [2] Schubert and Soderlund (2011); [3] Stacey (2007); [4] French et al. (2012); [5] Hauck et al. (2006); [6] Hanel et al. (1983); [7] Hubbard et al. (1995); [8] Mulford et al. (2014). Unlabeled values are original estimates.

Planet	α_T (K^{-1})	ρ [2] ($kg\,m^{-3}$)	ν [2] ($m^2\,s^{-1}$)	κ [2] ($m^2\,s^{-1}$)	C_p ($J\,kg^{-1}\,K^{-1}$)	Ω [2] (s^{-1})	g_0 ($m\,s^{-2}$)	R_P [2] (km)	R_D [2] (R_P)	L [2] (km)	q_{sa} ($W\,m^{-2}$)	$\lvert B_{r=R_D}\rvert$ [2] (μT)
Mercury	3×10^{-5} [1]	8000	10^{-6}	10^{-5}	800	1.2×10^{-6}	4 [1]	2440	0.75	610	0.01 [1]	0.6
Earth	1.8×10^{-5} [3]	11 000	10^{-6}	10^{-5}	800 [3]	7.3×10^{-5}	11	6371	0.55	2300	0.065 [3]	270
Jupiter	10^{-4} [4]	2000	10^{-7}	10^{-6}	15 000 [4]	1.8×10^{-4}	25 [4]	69 911	0.95	52 000	5.4 [4]	625
Ganymede	10^{-4} [5]	6000	10^{-6}	10^{-5}	10 000	1.0×10^{-5}	1.3	2634	0.3	530	0.003 [5]	32
Saturn	10^{-4}	2000	10^{-7}	10^{-7}	15 000	1.6×10^{-4}	15	58 232	0.5	15 000	2 [6]	45
Uranus	10^{-4}	2000	10^{-6}	10^{-7}	10 000 [8]	10^{-4}	9	25 362	0.8	5100	0.43 [7]	75
Neptune	10^{-4} [7]	2000	10^{-6}	10^{-7}	10 000 [8]	1.1×10^{-4}	11	24 624	0.8	12 000	0.042 [7]	73

Table 2
Non-dimensional parameter estimates for solar system planets used in Section 2. The flux Rayleigh number, $Ra_F = NuRa$, is estimated using the parameters given in Table 1. The estimates for Nu and Ra are performed by calculating the intersection between $Nu = Ra_F/Ra$ and a Nu–Ra scaling law, following the method in Section 6 of Cheng et al. (2015). Two different Nu–Ra scaling laws are used: The 'diffusion-free' estimate, denoted by $|_{df}$, corresponds to Christensen and Aubert (2006)'s $\beta^* = 0.53$ scaling converted to Nu–Ra coordinates. The 'rotating convection' estimate, denoted by $|_{rc}$, corresponds to $\alpha = 3.5$, the steepest rotating convection scaling law observed in Cheng et al. (2015). The critical Rayleigh number is given by (9) with $c_1 = 3.5$, corresponding to the predicted prefactor for a spherical shell geometry from King et al. (2010). The Elsasser number, Λ, is the ratio between Lorentz and Coriolis forces, defined here as $\Lambda = \sigma B_D^2/(\rho\Omega)$ where σ is the magnetic conductivity.

					Diffusion-free			Rotating convection			
Planet	E [2]	Pr [2]	Ra_F	Ra_Q^*	$Ra\lvert_{df}$	$Ra\lvert_{df}/Ra_{crit}$	$Nu\lvert_{df}$	$Ra\lvert_{rc}$	$Ra\lvert_{rc}/Ra_{crit}$	$Nu\lvert_{rc}$	Λ
Mercury	10^{-12}	0.1	1.6×10^{26}	1.6×10^{-8}	2.8×10^{20}	8.1×10^{3}	5.6×10^{5}	4.9×10^{18}	140	3.3×10^{7}	3.0×10^{-5}
Earth	10^{-15}	0.1	4.0×10^{29}	4.0×10^{-14}	6.6×10^{23}	1.9×10^{3}	6.0×10^{5}	3.6×10^{22}	100	1.1×10^{7}	0.072
Jupiter	10^{-19}	0.1	3.4×10^{40}	3.4×10^{-15}	2.1×10^{31}	2.8×10^{5}	1.6×10^{9}	1.4×10^{29}	1.8×10^{3}	2.5×10^{11}	0.86
Ganymede	10^{-13}	0.1	3.8×10^{25}	1.7×10^{-12}	5.7×10^{20}	510	6.8×10^{4}	3.9×10^{19}	43	9.8×10^{5}	0.014
Saturn	10^{-18}	0.1	3.0×10^{36}	4.5×10^{-15}	6.7×10^{28}	6.8×10^{4}	4.5×10^{7}	1.6×10^{27}	820	1.9×10^{9}	5×10^{-3}
Uranus	10^{-16}	10	8.5×10^{34}	1.3×10^{-14}	1.1×10^{27}	5.2×10^{5}	7.8×10^{7}	6.0×10^{24}	1.5×10^{3}	1.4×10^{10}	2.2×10^{-4}
Neptune	10^{-16}	10	3.5×10^{35}	5.3×10^{-14}	2.1×10^{27}	1.0×10^{6}	1.6×10^{8}	8.2×10^{24}	2.0×10^{3}	4.3×10^{10}	1.9×10^{-4}

the inertial forces are overly large, the heat transfer scaling deviates to a shallower trend associated with nonrotating convection (Soderlund et al., 2012). Arguably, this transition occurs at $Ra_T \simeq E^{-3/2}$ (e.g., King et al., 2012; Ecke and Niemela, 2014; Cheng et al., 2015). All dynamo data considered for the scaling arguments in Christensen and Aubert (2006) occur prior to the transition in heat transfer behavior (i.e., $Ra < Ra_T$). The shallower nonrotating trend is therefore not shown in Fig. 1a.

In the vast majority of rotating convection studies, the goal is to collapse different E-datasets via a physically-based set of arguments (e.g., Aubert et al., 2001; Schmitz and Tilgner, 2009; King et al., 2012; Julien et al., 2012b; Stellmach et al., 2014). If, instead, one were to perform a single fit to all the data from the compilation of the different E-datasets, this would yield a 'composite' best fit trend with a power law exponent that we refer to as β. In Fig. 1a, the composite fit trend is represented by the wide dashed line. This $\beta = 0.01$ trend gives a notably poor fit, having a coefficient of determination, R^2, of 0.004. This implies that β has no inherent physical meaning in describing the heat transfer. Instead, it is α that contains the physical information relevant to the systems convection dynamics (e.g., King et al., 2012; Cheng et al., 2015).

2.2. Diffusion-free parameters

At planetary scales, it is hypothesized that the physics becomes independent of the viscous, thermal and magnetic diffusive time scales. In Tables 1 and 2, we estimate the heat transfer parameters for dynamo-generating bodies in the solar system. These rough estimates give $Nu > 10^5$, $Ra > 10^{18}$ and $E \leq 10^{-12}$ for all of the bodies, indicating that the diffusive time scales are always extremely long compared to buoyant and rotational time scales. Thus, comparing buoyant and rotational time scales may better characterize the fluid physics in such systems (e.g., Fernando et al., 1991; Stevens et al., 2013). Towards this end, Christensen and Aubert (2006) define analogous diffusivity-free control parameters to the Nusselt and Rayleigh numbers by replacing the diffusive time scales with the rotational time scale $\tau_\Omega = \Omega^{-1}$.

The modified Rayleigh number, Ra^*, is defined in Christensen and Aubert (2006) by replacing both thermal and diffusive time scales with the rotational time scale in the definition of Ra:

$$Ra^* = Ra\frac{\tau_\Omega}{\tau_\nu}\frac{\tau_\Omega}{\tau_\kappa} = \left(\frac{\tau_\Omega}{\tau_{ff}}\right)^2 = \frac{\alpha_T g \Delta T}{\Omega^2 L} = \frac{RaE^2}{Pr}. \tag{11}$$

This parameter is the square of the convective Rossby number, $Ro_C = \tau_\Omega/\tau_{ff}$, a control parameter used in a broad array of rotating convection studies (e.g., Gilman, 1977; Gastine et al., 2013; King and Aurnou, 2013; Stevens et al., 2013; Ribeiro et al., 2015).

The diffusion-free modified Nusselt number is defined as the ratio between the rotational time scale and the convective heat flux time scale. As defined in (7), Nu is the ratio between the conductive heat flux time scale and the total heat flux time scale. Christensen and Aubert (2006) arrive at their modified Nusselt definition by first substituting $Nu - 1$ for Nu to compare the conductive heat flux time scale to the convective heat flux time scale. They then multiply this by the ratio of the rotational time scale to the conductive heat flux time scale:

$$Nu^* = (Nu-1)\frac{\tau_\Omega}{\tau_\kappa} = \frac{(Nu-1)E}{Pr} = \frac{q_{conv}}{\rho C_p \Delta T \Omega L} \tag{12}$$

where q_{conv} is the convective component of the total heat flux. This represents the ratio of the rotational time scale to the time for fluid to convectively transfer heat across the fluid layer.

Christensen and Aubert (2006), in turn, plot their data in terms of a modified flux Rayleigh number, Ra_Q^* which is defined as:

$$Ra_Q^* = Ra^* Nu^* = \frac{(Nu-1)RaE^3}{Pr^2} = \frac{\alpha_T g q_{conv}}{\rho C_p \Omega^3 L^2}. \tag{13}$$

As the modified Rayleigh number Ra^* is a convective Rossby number relating the rotation to buoyancy time scales, the flux

modified Rayleigh number Ra_Q^* is effectively a flux convective Rossby number. Other studies have also used this quantity as a control parameter for characterizing rotating convection regimes (e.g., Maxworthy and Narimousa, 1994; Jacobs and Ivey, 1999; Aurnou et al., 2003).

In Fig. 1b, we plot the same data shown in Fig. 1a, but now in the diffusion-free Nu^*–Ra_Q^* parameter space. Similar to Fig. 1a, data at a given Ekman number follow a power law scaling of:

$$Nu^* = c_2 Ra_Q^{*\alpha^*} \quad \text{(single } E \text{ scaling)}. \tag{14}$$

This α^* slope is a diffusion-free analogue to the α-slope in Fig. 1a. The composite fit over multiple Ekman numbers here is described by:

$$Nu^* = c_3 Ra_Q^{*\beta^*} \quad \text{(multiple } E, \text{ composite scaling)}. \tag{15}$$

This is denoted by the wide dashed line, analogous to the β-fit in Fig. 1a. In contrast to Fig. 1a, the data appear to collapse to a single trend in Nu^*–Ra_Q^* space and are well-described by $\beta^* = 0.63$, with an R^2 value of 0.98.

Fig. 1a shows that, in Nu–Ra space, the onset of convection occurs at a fixed $Nu = 1$ value regardless of the Ra_{crit} value. In contrast, the onset value of the modified Nusselt number varies as a function of E and Pr. Since $Nu - 1 = 0$ at onset, the onset of convection cannot be directly plotted in Nu^*–Ra_Q^* space. However, the onset scaling properties can be expressed as:

$$Nu|^*_{crit} \sim EPr^{-1},$$
$$Ra_Q|^*_{crit} \sim Ra_{crit} E^3 Pr^{-2} \sim E^{5/3} Pr^{-2}.$$

The majority of dynamo models included for this study are carried out at a fixed $Pr = 1$, giving:

$$Nu|^*_{crit} \sim E, \quad Ra_Q|^*_{crit} \sim E^{5/3}$$
$$\rightarrow Nu|^*_{crit} \sim (Ra_Q|^*_{crit})^{3/5}. \tag{16}$$

We see in this Nu^*–Ra_Q^* relationship that this corresponds to $\beta^*_{crit} = 3/5 = 0.6$ (Aurnou, 2007). Therefore, we predict that a viscous onset scaling, following this β^*_{crit} trend, will be apparent in all heat transfer plots using diffusion-free parameters. The viscous onset trend (16) is represented by the solid line in Fig. 1b.

3. Geometric scaling effects in diffusion-free parameter space

The composite best-fit slope in Nu–Ra space, β, appears effectively meaningless for describing the data, while the composite best-fit slope in Nu^*–$Ra_Q^{*\beta^*}$ appears to describe an overall trend in the data. The distinction between these two slopes is troubling because both are arrived at through the same argument and should therefore explain the same physical phenomena. We demonstrate here that, rather than conveying a physic argument, the goodness of fit of the composite scaling, β^*, is a geometric effect introduced by the usage of diffusion-free parameters. In particular, converting data to diffusion-free parameter space causes them to be flattened and stretched along the onset scaling slope, $\beta^*_{crit} = 0.6$, causing the onset scaling itself to appear as a good fit for all of the data.

In Fig. 2, we show composite fit values, β^*, to synthetic datasets that include differing numbers of E-datasets. The filled squares denote E-datasets with slope values fixed at $\alpha = 3.5$ and the hollow diamonds denote E-datasets with rather disparate slope values fixed at $\alpha = 0.5$. Each E-dataset contains ten equidistant data points between $Nu = 1$ and $Nu = 10$. As the number of E-datasets increases, the value of the composite scaling trend β^* quickly approaches the onset slope of 3/5, regardless of the α^* value. The β^* values collapse to within 10% of the onset scaling exponent once

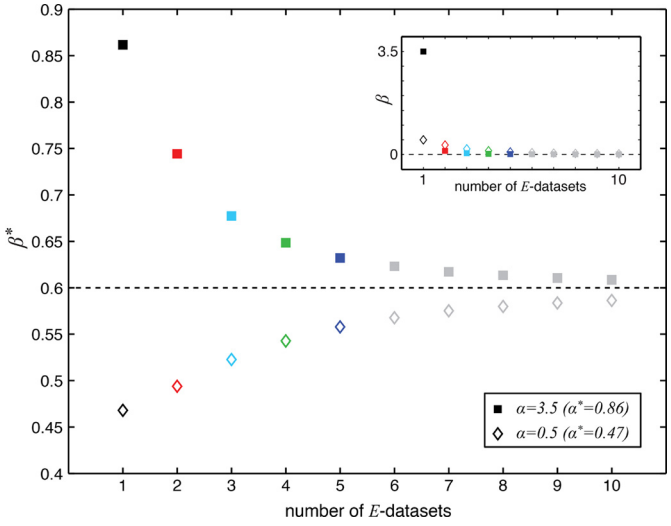

Fig. 2. Composite fit scaling exponent in diffusion-free parameter space, β^*, plotted versus the number of Ekman number datasets (a.k.a. "shingles") included in the fit. 'Number of E-datasets = 1' is associated with a single dataset at $E = 3 \times 10^{-4}$. Each dataset contains ten evenly-spaced data points in the range $1 < Nu < 10$ and each additional dataset decreases in Ekman value, down to $E = 10^{-8}$ for the tenth dataset. The colors of the bullet points correspond to the minimum E value included in the fit. The filled squares represent a Nu–Ra scaling exponent of $\alpha = 3.5$ while the hollow diamonds represent a Nu–Ra scaling exponent of $\alpha = 0.5$ (corresponding to fixed α^* values of 0.86 and 0.47, respectively). As more Ekman numbers are considered in the fit, the associated β^* values approach the onset value of 0.6. The inset shows the same data in diffusive parameter space, plotted as composite fit scaling β versus number of E-datasets included in the fit. Just like in diffusion-free space, the β values approach the onset value, 0 in this case, as more E-datasets are included. (For interpretation of the references to color in this figure legend, the reader is referred to the web version of this article.)

five or more E-datasets are included in the fit. The inset demonstrates that exactly the same behavior is true for β in Nu–Ra space: just as in the diffusion-free case, the composite fit quickly approaches the onset scaling exponent of 0, regardless of the α value. This demonstrates that the diffusion-free heat transfer trend β^* is just a stretched, rotated version of the diffusive composite trend β. Neither β or β^*, though, are meaningful; the physically relevant heat transfer information resides in the scaling exponents α.

Now let us compare the behaviors of α versus α^*. In Fig. 1a, the synthetic data span a total of $\simeq 3$ orders of magnitude in Ra and $\simeq 1$ order of magnitude in Nu. In Fig. 1b, the same data span $\simeq 5$ orders of magnitude in Ra_Q^* and $\simeq 3$ orders of magnitude in Nu^*. This difference is primarily explained by the strong viscous onset trend. However, there is an important secondary "flattening" effect due to the relationship between α and α^*. While the two α values in Fig. 2 differ by a factor of 7, the associated α^* values only differ by a factor of 1.8. For sufficiently high Nu, such that $Nu - 1 \approx Nu$, the value of α^* is directly related to α:

$$Nu^* \sim Nu \sim Ra^{\alpha}, \quad Ra_Q^{*\alpha^*} \sim (NuRa)^{\alpha^*} \sim Ra^{(\alpha+1)\alpha^*};$$
$$Nu^* \sim Ra_Q^{*\alpha^*} \rightarrow \alpha = \alpha^*(\alpha + 1)$$
$$\rightarrow \alpha^* = \frac{\alpha}{\alpha + 1}. \tag{17}$$

Fig. 3 plots the relationship given in (17) over the range $\alpha =$ (0 to 10). The plot demonstrates that for any value of α, the associated value of α^* will necessarily exist in the range [0; 1]. The red dashed lines indicate $\alpha^* = \beta^*_{crit} = 3/5$ and the corresponding value of $\alpha = 3/2$. For all $\alpha < 3/2$, α^* is smaller than β^*_{crit} leading to shingles with shallower slopes than the onset scaling. For all $\alpha > 3/2$, α^* is greater than β^*_{crit} leading to shingles with steeper slopes than the onset scaling. Thus, for steep slopes such as $\alpha = 3.5$ observed in rotating convection experiments (Cheng et al., 2015), differences

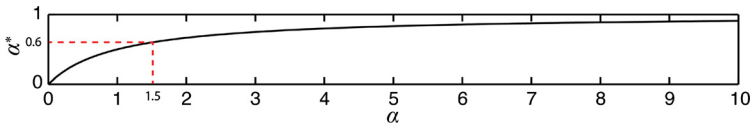

Fig. 3. Plot of the slope of an E-dataset in Nu^*–Ra_Q^* space (α^*) versus the slope of an E-dataset in Nu–Ra space (α). These slopes are related by $\alpha^* = \alpha/(\alpha+1)$. The red dashed lines demarcate the slope of the onset scaling, $\alpha^* = \beta^*_{crit} = 3/5$, and the corresponding scaling in diffusive parameters, $\alpha = 1.5$.

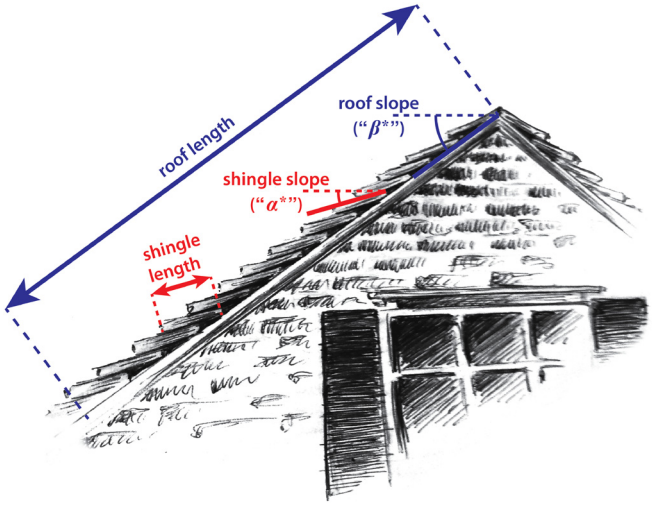

Fig. 4. Schematic showing the 'shingling' effect that occurs when heat transfer data are plotted in diffusion-free parameter space. The roof slope is analogous to the viscously controlled onset scaling given in (16). The shingles each represent a different E-dataset. The slope of an individual shingle is analogous to α^*. The best-fit slope through a number of shingles is analogous to the composite fit β^*. When enough shingles are included in the fit, the slope of each shingle has no effect on the overall composite slope. The composite fit therefore approaches the slope of the roof. This is analogous to the way in which the diffusion-free data must approach the viscously-controlled onset scaling (16) given a sufficiently large number of E-datasets.

in α are significantly less pronounced when converted to α^*. We refer to this as the "flattening" effect on heat transfer data when converting from diffusive to diffusion-free parameter space.

Fig. 4 schematically illustrates the essential diffusion-free behaviors that arise in Figs. 1b and 2. Plotting heat transfer data in diffusion-free parameter space results in an effect we call "shingling." The roof of a house is used as an analogy to demonstrate this effect. The slope of the roof corresponds to the onset scaling $Nu|^*_{crit} \sim (Ra_Q|^*_{crit})^{\beta^*_{crit}}$. The slopes of the shingles on the roof, analogous to α^*, differ from the roof slope. Importantly, the length of each shingle is significantly shorter than the total roof length. We describe the roof length using the maximum Ra value over the minimum Ra value over all E values, and the shingle length using the maximum Ra value over the minimum Ra value for a single E value. For the full range of data in Fig. 1, $Ra_{max}/Ra_{min} = 380$. In contrast, for each individual E-dataset shingle, $Ra_{max}/Ra_{min} < 10$. In addition, the flattening effect described in (17) causes each shingle to lie flat against the roof. With a large number of flat, short shingles lining the roof, the overall observed slope corresponds to only the slope of the roof, even though the physically significant quantity is the slope of each shingle. Thus, the shingling and flattening effects, which are inherent to the diffusion-free representation, obscure the physically relevant scalings in favor of the onset scaling.

It is important to note, following Julien et al. (2012a), that the heat transfer can indeed be argued to be free of the effects of fluid diffusivities should the α value asymptote to 3/2 as the data approach extreme parameter values (e.g., $E \to 0$ and $Ra \gg Ra_{crit}$). However, this behavior is not yet found in present day dynamo data (see Fig. 5b below) or rotating convection data (e.g., Stellmach et al., 2014; Aurnou et al., 2015; Cheng et al., 2015).

Summarizing Fig. 4, our shingling arguments imply that the viscous onset scaling controls the composite trend of the data in diffusion-free parameter space. Further, the flattening effect makes each E-dataset's "shingle" appear to have roughly the same slope, homogenizing almost any data to appear nearly identical when represented in this way.

4. Dynamo data

In Fig. 5, we demonstrate that the flattening and shingling effects are responsible for the goodness of the composite fit of dynamo data in diffusion-free parameter space by plotting numerical dynamo data from Christensen et al. (1999) and Christensen and Aubert (2006) using both diffusive parameters (Fig. 5a) and diffusion-free parameters (Fig. 5c).

The individual slopes, α, of the E-datasets vary significantly in diffusive parameter space (Fig. 5a). This is quantified in Fig. 5b: the slope α increases monotonically from 0.44 to 1.08 as the value of the Ekman number changes from 10^{-3} to 3×10^{-6}. Comparable trends in α values are found in rotating convection data between $E = 10^{-5}$ and 10^{-7} in water (Cheng et al., 2015).

In diffusion-free parameter space, these data conform closely to a single value of α^*. In Fig. 5d the mean α^* value is shown to be 0.53 with variance of <0.05. A composite fit of $\beta^* = 0.53$ ($R^2 = 0.998$) therefore appears appropriate for describing all the dynamo data. However, unlike the steepening scaling in Nu–Ra space, the slopes in Nu^*–Ra_Q^* are all within 5% of 0.53. This demonstrates that essential scaling information, which is present in the diffusive representation, has been lost in the transition to diffusion-free parameter space due to the flattening and shingling phenomena described above. Because datasets that follow different scaling exponents are flattened to very similar values in diffusion-free space, plotting these datasets together gives the impression of a single slope. Taking a composite fit to all these flattened datasets gives a β^* value that is comparable to the onset scaling $\beta^*_{crit} = 0.6$ from (16).

The 12% difference between $\beta^* = 0.53$ and $\beta^*_{crit} = 0.6$ exists because of the increasing minimum Nu value as E is decreased in Fig. 5a; each of Christensen and Aubert (2006)'s E-datasets begins at a higher value of Ra/Ra_{crit}. This is done in order to omit the shallow "tail" that occurs in spherical shell geometries near onset due to the convection not being space-filling (e.g., Gillet and Jones, 2006; Yadav et al., 2015). In Nu–Ra space, the total envelope of data slopes upward as Ra increases. Analogously, in Nu^*–Ra_Q^* space, the total envelope of data slopes upward as Ra_Q^* *decreases*, leading to a shallower scaling and a smaller value of β^*. Thus, the difference between the onset slope and the composite slope reported in Christensen and Aubert (2006) is predictable based on geometric (versus physical) considerations.

5. Summary

In this study, we have shown that heat transfer, plotted in diffusion-free parameter space, is controlled by viscous diffusivity of the fluid, in qualitative agreement with the viscous length-scale arguments put forward in King and Buffett (2013). Irrespective of

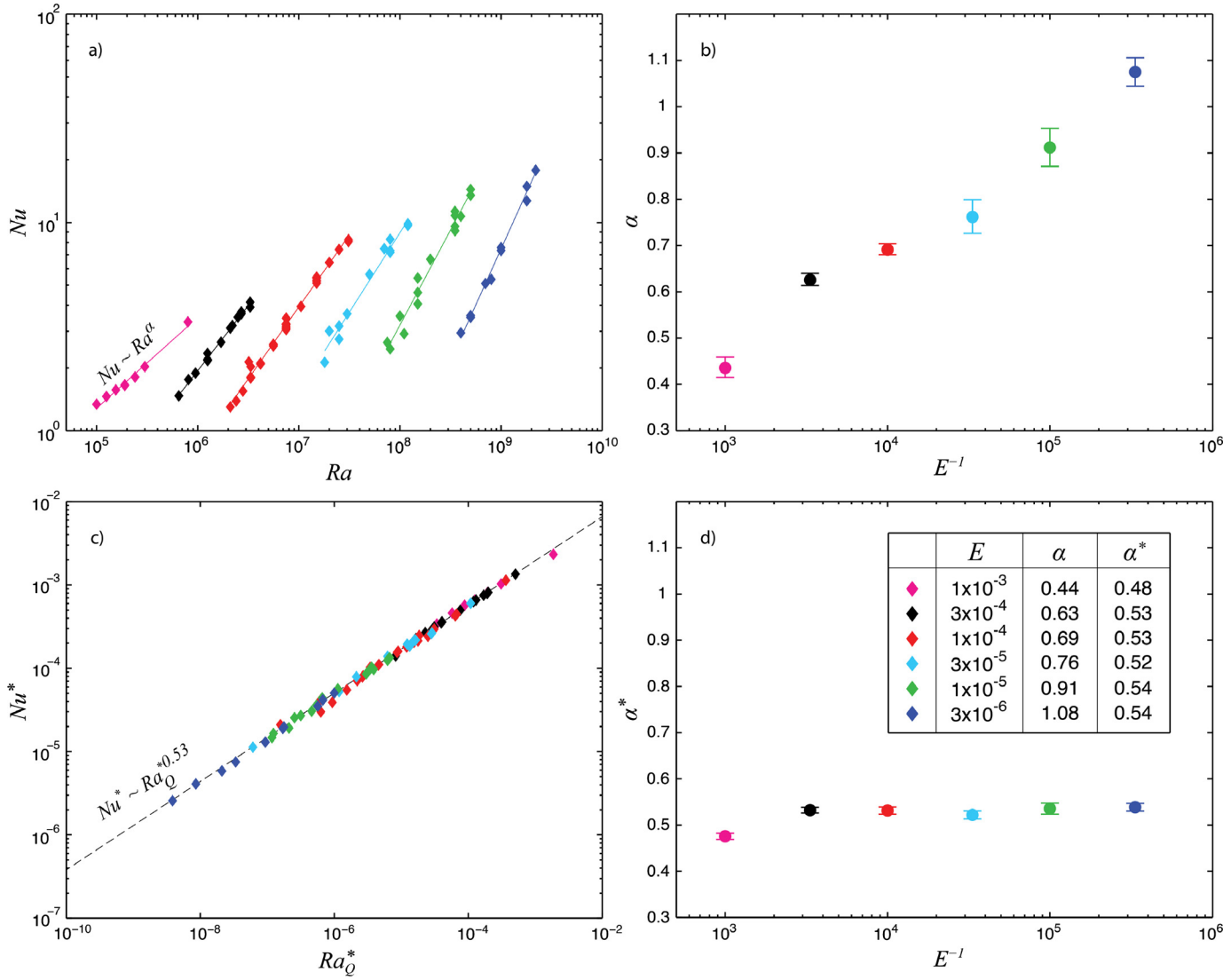

Fig. 5. Numerical dynamo heat transfer data from Christensen et al. (1999) and Christensen and Aubert (2006) plotted using diffusive (a, b) and diffusion-free (c, d) parameters. a) *Nu* versus *Ra* heat transfer data. b) Best fit scaling exponent α for each E-dataset (a.k.a. for each 'shingle'). A clear trend in the value of α exists as the value of E decreases. c) Diffusion-free heat transfer Nu^* vs. diffusion-free buoyancy forcing Ra_Q^*. Here, the data appear to align with a single composite slope, $\beta^* = 0.53$. d) Best fit diffusion-free scaling exponent α^* versus E^{-1}. The identical data shown in Fig. 5b are strongly flattened in diffusion-free parameter space, following (17); the α^*-values show no significant variation as a function of E.

the input trend α found at each individual Ekman number, Fig. 2 demonstrates that the supposedly diffusion-free β^* value must approach the viscously-controlled onset scaling value of 3/5, so long as sufficiently many Ekman numbers are included. Furthermore, since the 3/5 scaling is associated with the onset of rotating convection, this may indicate that Lorentz forces only weakly affect the convection processes in Christensen and Aubert (2006)'s dynamo data (e.g., Soderlund et al., 2012, 2015). Thus, we stress that the β^* scaling is hydrodynamic in nature and is controlled by the viscous onset of convection. This viscously-controlled behavior then contradicts the idea that the diffusion-free composite fit β^* provides geophysically-relevant scaling information.

Since diffusion-free heat transfer data appears to collapse nearly perfectly (Fig. 5), it is argued that diffusivities have indeed dropped out of the problem. However, we have shown here that exactly the opposite is true: The diffusion-free β^* trend instead reveals that this is the viscously-controlled onset trend for nonmagnetic rotating convection. This raises a separate fundamental point, which is that by removing all diffusivities *a priori* from the parameters, it becomes difficult, or even impossible, to test whether diffusivities matter (cf. Julien et al., 2012a; Featherstone and Hindman, 2015). Any scaling – even viscously-controlled onset – appears to result from a diffusion-free process if the starting assumption is to remove all the diffusivities from the control parameters.

Our findings are relevant to our interpretation and understanding of present day dynamo modeling results. Our results demonstrate that the viscous diffusivity, via the onset conditions, plays a key role in determining supposedly diffusion-free behaviors of the system. Thus, Christensen and Aubert (2006)'s diffusion-free heat transfer scalings are likely only valid in geophysical settings in which dynamo action is occurring very near to the onset of convection ($Ra \simeq Ra_{crit}$). However, our Ra/Ra_{crit} estimates in Table 2 do not support this contention. Instead, these estimates indicate that convection in dynamo-generating regions is strongly supercritical in most solar system bodies. Since presently-available dynamo data do not provide support for diffusion-free physics, it still remains to be determined under what conditions, if any, dynamo generation becomes free of fluid diffusivities. Next generation models that incorporate advanced dynamo physics (e.g., Calkins et al., 2015) and advanced parallelization capabilities (e.g., Nataf and Schaeffer,

2015) may prove capable of reaching the hypothesized diffusion-free regime.

Acknowledgements

The authors gratefully acknowledge support provided by the US NSF Geophysics Program under CSEDI award #1067944 and EAR award #1246861. We also thank Bruce Buffett and two anonymous referees as well as K. Julien, E.M. King, P.H. Roberts and K.M. Soderlund for feedback that greatly improved the manuscript.

References

Ahlers, G., Grossman, S., Lohse, D., 2009. Heat transfer and large scale dynamics in turbulent Rayleigh–Bénard convection. Rev. Mod. Phys. 81, 503–537.
Aubert, J., Aurnou, J., Wicht, J., 2008. The magnetic structure of convection-driven numerical dynamos. Geophys. J. Int. 172 (3), 945–956.
Aubert, J., Brito, D., Nataf, H.-C., Cardin, P., Masson, J.-P., 2001. A systematic experimental study of rapidly rotating spherical convection in water and liquid gallium. Phys. Earth Planet. Inter. 128 (1), 51–74.
Aubert, J., Labrosse, S., Poitou, C., 2009. Modelling the palaeo-evolution of the geodynamo. Geophys. J. Int. 179 (3), 1414–1428.
Aubert, J., Tarduno, J.A., Johnson, C.L., 2010. Observations and models of the long-term evolution of Earths magnetic field. Space Sci. Rev. 155 (1–4), 337–370.
Aurnou, J., 2007. Planetary core dynamics and convective heat transfer scaling. Geophys. Astrophys. Fluid Dyn. 101, 327–345.
Aurnou, J., Andreadis, S., Zhu, L., Olson, P., 2003. Experiments on convection in Earth's core tangent cylinder. Earth Planet. Sci. Lett. 212, 119–134.
Aurnou, J., Aubert, J., 2011. End-member models of boundary-modulated convective dynamos. Phys. Earth Planet. Inter. 187, 353–363.
Aurnou, J., Calkins, M., Cheng, J., Julien, K., King, E., Nieves, D., Soderlund, K., Stellmach, S., 2015. Rotating convective turbulence in Earth and planetary cores. Phys. Earth Planet. Inter. 246, 52–71.
Bergman, T., Incropera, F., Lavine, A., 2011. Fundamentals of Heat and Mass Transfer. John Wiley & Sons.
Calkins, M.A., Julien, K., Tobias, S.M., Aurnou, J.M., 2015. A multiscale dynamo model driven by quasi-geostrophic convection. J. Fluid Mech. 780, 143–166.
Chandrasekhar, S., 1961. Hydrodynamic and Hydromagnetic Stability, 1st edition. OUP.
Cheng, J., Stellmach, S., Ribeiro, A., Grannan, A., King, E., Aurnou, J., 2015. Laboratory-numerical models of rapidly rotating convection in planetary cores. Geophys. J. Int. 201, 1–17.
Christensen, U., 2002. Zonal flows driven by strongly supercritical convection in rotating spherical shells. J. Fluid Mech. 470, 115–133.
Christensen, U., 2011. Geodynamo models: tools for understanding properties of Earth's magnetic field. Phys. Earth Planet. Inter. 187, 157–169.
Christensen, U., Aubert, J., 2006. Scaling properties of convection-driven dynamos in rotating spherical shells and application to planetary magnetic fields. Geophys. J. Int. 166 (1), 97–114.
Christensen, U., Aubert, J., Hulot, G., 2010. Conditions for Earth-like geodynamo models. Earth Planet. Sci. Lett. 296, 487–496.
Christensen, U., Holzwarth, V., Reiners, A., 2009. Energy flux determines magnetic field strength of planets and stars. Nature 457 (7226), 167–169.
Christensen, U., Olson, P., Glatzmaier, G., 1999. Numerical modelling of the geodynamo: a systematic parameter study. Geophys. J. Int. 138 (2), 393–409.
Christensen, U.R., 2015. Iron snow dynamo models for Ganymede. Icarus 247, 248–259.
Davidson, P., 2013. Scaling laws for planetary dynamos. Geophys. J. Int. 195 (1), 67–74.
Davidson, P., 2014. The dynamics and scaling laws of planetary dynamos driven by inertial waves. Geophys. J. Int. 198 (3), 1832–1847.
Davies, C., Pozzo, M., Gubbins, D., Alfè, D., 2015. Constraints from material properties on the dynamics and evolution of Earth's core. Nat. Geosci. http://dx.doi.org/10.1038/ngeo2492.
Dharmaraj, G., Stanley, S., Qu, A., 2014. Scaling laws, force balances and dynamo generation mechanisms in numerical dynamo models: influence of boundary conditions. Geophys. J. Int. 199 (1), 514–532.
Driscoll, P., Bercovici, D., 2013. Divergent evolution of Earth and Venus: influence of degassing, tectonics, and magnetic fields. Icarus 226 (2), 1447–1464.
Driscoll, P., Olson, P., 2011. Optimal dynamos in the cores of terrestrial exoplanets: magnetic field generation and detectability. Icarus 213 (1), 12–23.
Ecke, R., Niemela, J., 2014. Heat transport in the geostrophic regime of rotating Rayleigh–Bénard convection. Phys. Rev. Lett. 113, 114301.
Featherstone, N.A., Hindman, B.W., 2015. The spectral amplitude of stellar convection and its scaling in the high-Rayleigh-number regime. arXiv:1511.02396.
Fernando, H., Chen, R.-R., Boyer, D., 1991. Effects of rotation on convective turbulence. J. Fluid Mech. 228, 513–547.
French, M., Becker, A., Lorenzen, W., Nettelmann, N., Bethkenhagen, M., Wicht, J., Redmer, R., 2012. Ab initio simulations for material properties along the Jupiter adiabat. Astrophys. J. Suppl. Ser. 202 (1), 5.
Gaidos, E., Conrad, C.P., Manga, M., Hernlund, J., 2010. Thermodynamic limits on magnetodynamos in rocky exoplanets. Astrophys. J. 718 (2), 596.
Garcia, F., Sánchez, J., Net, M., 2014. Numerical simulations of thermal convection in rotating spherical shells under laboratory conditions. Phys. Earth Planet. Inter. 230, 28–44
Gastine, T., Wicht, J., Aurnou, J., 2013. Zonal flow regimes in rotating anelastic spherical shells: an application to the giant planets. Icarus 225, 156–172.
Gillet, N., Jones, C., 2006. The quasi-geostrophic model for rapidly rotating spherical convection outside the tangent cylinder. J. Fluid Mech. 554, 343–369.
Gilman, P., 1977. Nonlinear dynamics of Boussinesq convection in a deep rotating spherical shell – I. Geophys. Astrophys. Fluid Dyn. 8 (1), 93–135.
Glatzmaier, G., 2013. Introduction to Modeling Convection in Planets and Stars: Magnetic Field, Density Stratification, Rotation. Princeton University Press.
Glatzmaier, G., Coe, R., 2007. Magnetic Polarity Reversals in the Core, 1st edition. Treatise on Geophysics, vol. 8. Elsevier, pp. 283–297.
Glazier, J., 1999. Evidence against 'ultrahard' thermal turbulence at very high Rayleigh numbers. Nature 398, 307–310.
Grossmann, S., Lohse, D., 2011. Multiple scaling in the ultimate regime of thermal convection. Phys. Fluids 23 (4), 045108.
Gubbins, D., Roberts, P., 1987. Magnetohydrodynamics of the Earth's core. In: Encyclopedia of Geomagnetism and Paleomagnetism, vol. 2. Springer, pp. 1–183.
Hanel, R., Conrath, B., Kunde, V., Pearl, J., Pirraglia, J., 1983. Albedo, internal heat flux, and energy balance of Saturn. Icarus 53 (2), 262–285.
Hauck, S.A., Aurnou, J.M., Dombard, A.J., 2006. Sulfur's impact on core evolution and magnetic field generation on Ganymede. J. Geophys. Res. 111 (E9).
He, X., Shang, X.-D., Tong, P., 2014. Test of the anomalous scaling of passive temperature fluctuations in turbulent Rayleigh–Bénard convection with spatial inhomogeneity. J. Fluid Mech. 753, 104–130.
Hubbard, W., Podolak, M., Stevenson, D., 1995. The interior of Neptune. In: Neptune and Triton, vol. 109. University of Arizona Press, Tucson, AZ.
Incropera, F., DeWitt, D., 1985. Introduction to Heat Transfer. John Wiley & Sons.
Jacobs, P., Ivey, G., 1999. Rossby number regimes for isolated convection in a homogeneous, rotating fluid. Dyn. Atmos. Ocean. 30 (2), 149–171.
Julien, K., Knobloch, E., Rubio, A., Vasil, G., 2012a. Heat transport in low-Rossby-number Rayleigh–Bénard convection. Phys. Rev. Lett. 109, 254503.
Julien, K., Rubio, A., Grooms, I., Knobloch, E., 2012b. Statistical and physical balances in low Rossby number Rayleigh–Bénard convection. Geophys. Astrophys. Fluid Dyn. 106, 254503.
King, E., Aurnou, J., 2013. Turbulent convection in liquid metal with and without rotation. Proc. Natl. Acad. Sci. USA 110 (17), 6688–6693.
King, E., Soderlund, K., Christensen, U., Wicht, J., Aurnou, J., 2010. Convective heat transfer in planetary dynamo models. Geochem. Geophys. Geosyst. 11. http://dx.doi.org/10.1029/2010GC003053.
King, E., Stellmach, S., Aurnou, J., 2012. Heat transfer by rapidly rotating Rayleigh–Bénard convection. J. Fluid Mech. 691, 568–582.
King, E.M., Buffett, B.A., 2013. Flow speeds and length scales in geodynamo models: the role of viscosity. Earth Planet. Sci. Lett. 371, 156–162.
Kraichnan, R., 1962. Turbulent thermal convection at arbitrary Prandtl number. Phys. Fluids 5 (11), 1374–1389.
Kutzner, C., Christensen, U., 2002. From stable dipolar towards reversing numerical dynamos. Phys. Earth Planet. Inter. 131 (1), 29–45.
Laneuville, M., Wieczorek, M., Breuer, D., Aubert, J., Morard, G., Rückriemen, T., 2014. A long-lived lunar dynamo powered by core crystallization. Earth Planet. Sci. Lett. 401, 251–260.
Maxworthy, T., Narimousa, S., 1994. Unsteady, turbulent convection into a homogeneous, rotating fluid, with oceanographic applications. J. Phys. Oceanogr. 24 (5), 865–887.
Mulford, R., Swift, D., Hamel, S., 2014. Equation of state of ammonia. J. Phys. Conf. Ser. 7, 072001.
Nataf, H.-C., Schaeffer, N., 2015. Turbulence in the Core, 2nd edition. Treatise on Geophysics, vol. 8. Elsevier, pp. 161–181.
Olson, P., Christensen, U., 2006. Dipole moment scaling for convection-driven planetary dynamos. Earth Planet. Sci. Lett. 250 (3), 561–571.
Olson, P., Glatzmaier, G., Coe, R., 2011. Complex polarity reversals in a geodynamo model. Earth Planet. Sci. Lett. 304 (1), 168–179.
Pozzo, M., Davies, C., Gubbins, D., Alfe, D., 2012. Thermal and electrical conductivity of iron at Earth's core conditions. Nature 485 (7398), 355–358.
Redmond, H., King, S., 2007. Does mantle convection currently exist on Mercury? Phys. Earth Planet. Inter. 164 (3), 221–231.
Ribeiro, A., Fabre, G., Guermond, J.-L., Aurnou, J., 2015. Canonical models of geophysical and astrophysical flows: turbulent convection experiments in liquid metals. Metals 5 (1), 289–335.
Roche, P.-E., Gauthier, F., Kaiser, R., Salort, J., 2010. On the triggering of the ultimate regime of convection. New J. Phys. 12 (8), 085014.
Schmitz, S., Tilgner, A., 2009. Heat transport in rotating convection without Ekman layers. Phys. Rev. E 80, 015305.

Schmitz, S., Tilgner, A., 2010. Transitions in turbulent rotating Rayleigh–Bénard convection. Geophys. Astrophys. Fluid Dyn. 104 (5–6), 481–489.
Schrinner, M., Petitdemange, L., Raynaud, R., Dormy, E., 2014. Topology and field strength in spherical, anelastic dynamo simulations. Astron. Astrophys. 564, A78.
Schubert, G., Soderlund, K., 2011. Planetary magnetic fields: observations and models. Phys. Earth Planet. Inter. 187, 92–108.
Showman, A., Kaspi, Y., Flierl, G., 2011. Scaling laws for convection and jet speeds in the giant planets. Icarus 211 (2), 1258–1273.
Soderlund, K., King, E., Aurnou, J., 2012. The influence of magnetic fields in planetary dynamo models. Earth Planet. Sci. Lett. 333, 9–20.
Soderlund, K.M., Sheyko, A., King, E.M., Aurnou, J.M., 2015. The competition between Lorentz and Coriolis forces in planetary dynamos. Prog. Earth Planet. Sci. 2 (1), 1–10.
Spiegel, E., 1971. Convection in stars. I. Basic Boussinesq convection. Annu. Rev. Astron. Astrophys. 9, 323–352.
Sreenivasan, B., Jones, C., 2011. Helicity generation and subcritical behavior in rapidly rotating dynamos. J. Fluid Mech. 688, 5–30.
Stacey, F.D., 2007. Core properties, physical. In: Encyclopedia of Geomagnetism and Paleomagnetism. Springer, pp. 91–94.
Stellmach, S., Lischper, M., Julien, K., Vasil, G., Cheng, J., Ribeiro, A., King, E., Aurnou, J., 2014. Approaching the asymptotic regime of rapidly rotating convection: boundary layers versus interior dynamics. Phys. Rev. Lett. 113, 254501.
Stelzer, Z., Jackson, A., 2013. Extracting scaling laws from numerical dynamo models. Geophys. J. Int. http://dx.doi.org/10.1093/gji/ggt083.
Stevens, R., Clercx, H., Lohse, D., 2013. Heat transport and flow structure in rotating Rayleigh–Bénard convection. Eur. J. Mech. B, Fluids 40, 41–49.
Summeren, J., Gaidos, E., Conrad, C.P., 2013. Magnetodynamo lifetimes for rocky, Earth-mass exoplanets with contrasting mantle convection regimes. J. Geophys. Res. 118 (E5), 938–951.
Takahashi, F., Matsushima, M., Honkura, Y., 2008. Scale variability in convection-driven MHD dynamos at low Ekman number. Phys. Earth Planet. Inter. 167, 168–178.
Tarduno, J.A., Cottrell, R.D., Nimmo, F., Hopkins, J., Voronov, J., Erickson, A., Blackman, E., Scott, E.R., McKinley, R., 2012. Evidence for a dynamo in the main group pallasite parent body. Science 338 (6109), 939–942.
Tilgner, A., 2014. Magnetic energy dissipation and mean magnetic field generation in planar convection-driven dynamos. Phys. Rev. E 90 (1), 013004.
Weiss, B., Gattacceca, J., Stanley, S., Rochette, P., Christensen, U., 2010. Paleomagnetic records of meteorites and early planetesimal differentiation. Space Sci. Rev. 152, 341–390.
Yadav, R., Gastine, T., Christensen, U., 2013a. Scaling laws in spherical shell dynamos with free-slip boundaries. Icarus 225 (1), 185–193.
Yadav, R.K., Gastine, T., Christensen, U.R., Duarte, L.D., 2013b. Consistent scaling laws in anelastic spherical shell dynamos. Astrophys. J. 774 (1), 6.
Yadav, R., Gastine, T., Christensen, U., Duarte, L., Reiners, A., 2015. Effect of shear and magnetic field on the heat-transfer efficiency of convection in rotating spherical shells. arXiv:1507.03649.
Zhang, P., Cohen, R., Haule, K., 2015. Effects of electron correlations on transport properties of iron at Earth's core conditions. Nature 517 (7536), 605–607.
Zuluaga, J.I., Bustamante, S., Cuartas, P.A., Hoyos, J.H., 2013. The influence of thermal evolution in the magnetic protection of terrestrial planets. Astrophys. J. 770 (1), 23.

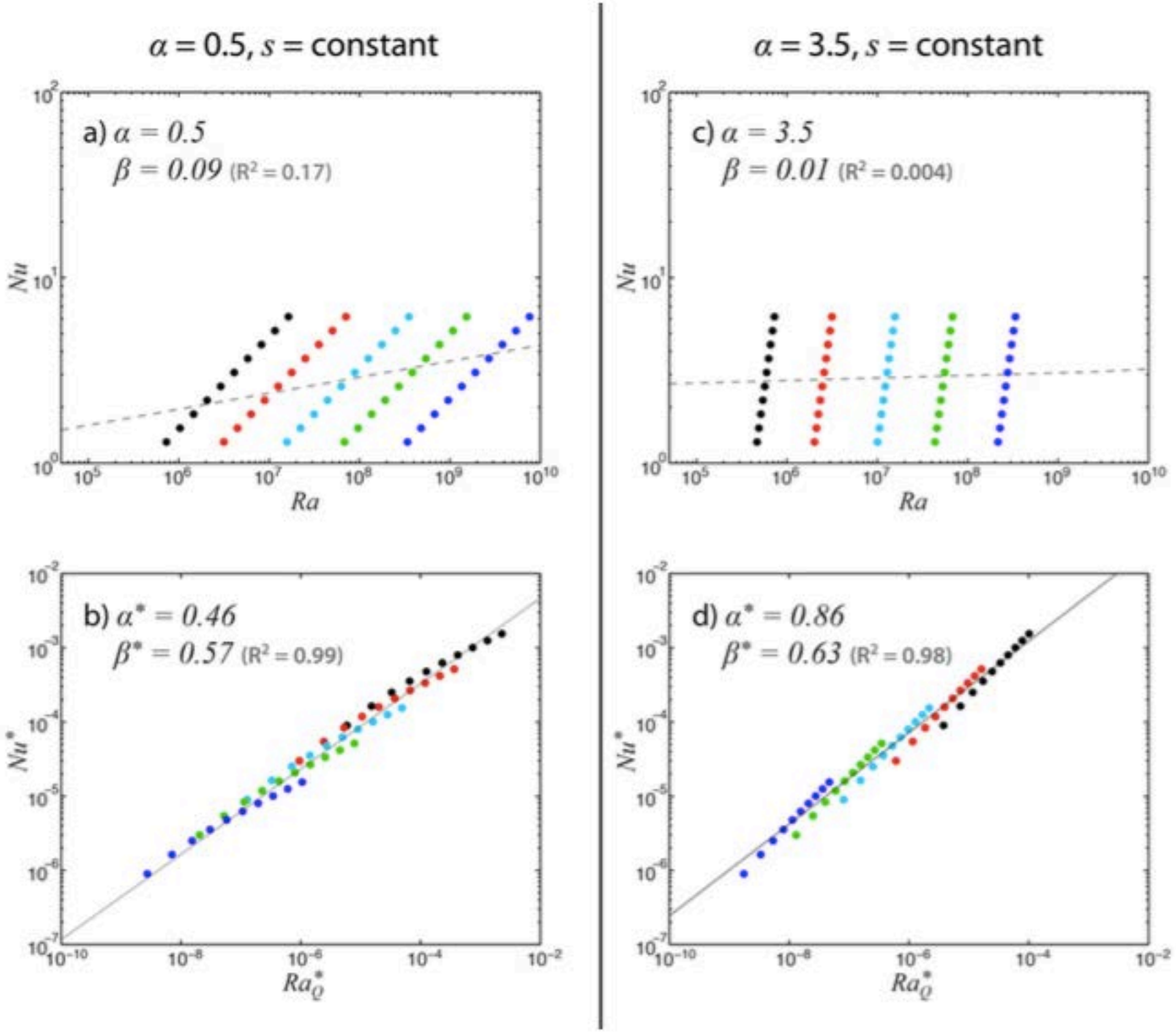
$\alpha = 0.5, s = \text{constant}$
$\alpha = 3.5, s = \text{constant}$
a) $\alpha = 0.5$
$\beta = 0.09$ ($R^2 = 0.17$)
c) $\alpha = 3.5$
$\beta = 0.01$ ($R^2 = 0.004$)
Nu
Ra
b) $\alpha^* = 0.46$
$\beta^* = 0.57$ ($R^2 = 0.99$)
d) $\alpha^* = 0.86$
$\beta^* = 0.63$ ($R^2 = 0.98$)
Nu^*
Ra_Q^*